



# Synthesis and characterization of $\text{TiB}_x$ ( $1.2 \leq x \leq 2.8$ ) thin films grown by DC magnetron co-sputtering from $\text{TiB}_2$ and Ti targets

Niklas Hellgren<sup>a,\*</sup>, Alexander Sredenschek<sup>a,1</sup>, Andrejs Petruins<sup>b</sup>, Justinas Palisaitis<sup>c</sup>,  
Fedor F. Klimashin<sup>b,2</sup>, Mauricio A. Sortica<sup>d</sup>, Lars Hultman<sup>c</sup>, Per O.Å. Persson<sup>c</sup>,  
Johanna Rosen<sup>b,\*</sup>

<sup>a</sup> Department of Computing, Mathematics, and Physics, Messiah University, Mechanicsburg, PA 17055, USA

<sup>b</sup> Materials Design Division, Department of Physics (IFM), Linköping University, SE-58183 Linköping, Sweden

<sup>c</sup> Thin Film Physics Division, Department of Physics (IFM), Linköping University, SE-58183 Linköping, Sweden

<sup>d</sup> Tandem Laboratory, Uppsala University, Box 529, SE-75120 Uppsala, Sweden

## ARTICLE INFO

### Keywords:

Titanium diboride  
Magnetron co-sputtering  
Annealing  
Stoichiometry  
Microstructure

## ABSTRACT

Titanium boride,  $\text{TiB}_x$ , thin films were grown by direct current magnetron co-sputtering from a compound  $\text{TiB}_2$  target and a Ti target at an Ar pressure of 2.2 mTorr (0.3 Pa) and substrate temperature of 450 °C. While keeping the power of the  $\text{TiB}_2$  target constant at 250 W, and by varying the power on the Ti target,  $P_{\text{Ti}}$ , between 0 and 100 W, the B/Ti ratio in the film could be continuously and controllably varied from 1.2 to 2.8, with close-to-stoichiometric diboride films achieved for  $P_{\text{Ti}} = 50$  W. This was done without altering the deposition pressure, which is otherwise the main modulator for the composition of magnetron sputtered  $\text{TiB}_x$  diboride thin films. The film structure and properties of the as-deposited films were compared to those after vacuum-annealing for 2 h at 1100 °C. As-deposited films consisted of small ( $\leq 50$  nm) randomly oriented  $\text{TiB}_2$  crystallites, interspersed in an amorphous, sometimes porous tissue phase. Upon annealing, some of the tissue phase crystallized, but the diboride average grain size did not change noticeably. The near-stoichiometric film had the lowest resistivity, 122  $\mu\Omega\text{cm}$ , after annealing. Although this film had growth-induced porosity, an interconnected network of elongated crystallites provides a path for conduction. All films exhibited high hardness, in the 25–30 GPa range, where the highest value of  $\sim 32$  GPa was obtained for the most Ti-rich film after annealing. This film had the highest density and was nano-crystalline, where dislocation propagation is interrupted by the off-stoichiometric grain boundaries.

## 1. Introduction

Titanium diboride  $\text{TiB}_2$ , is a ceramic material that has attracted considerable attention due to its distinctive properties, including high hardness [1–3], good electrical and thermal conductivity [4–6], as well as excellent thermal and chemical stability [7,8]. Consequently, thin films of this compound have been explored for a variety of applications, such as cutting tools, dies, and engine components [9–13]. Numerous techniques have been utilized for  $\text{TiB}_x$  ( $x$  varied around 2) thin film deposition, the most prevalent being direct-current magnetron sputtering (DCMS) from a compound  $\text{TiB}_2$  target in Ar atmosphere [3,14–19].

However, the difficulties of controlling the film stoichiometry with DCMS have been well documented [3,14,16–19]. In most cases, strongly over-stoichiometric films have been reported, with B/Ti ratios ranging from  $\sim 2.4$  to 3.5, rather than 2.0 as would be expected from a stoichiometric target. Only at elevated pressures and/or long target-to-substrate distances, does the film stoichiometry approach that of the target. Neidhardt et al. [16] explained this in terms of different ejection angles of the sputtered B and Ti atoms; B being emitted primarily in the target normal direction, while Ti is emitted more toward the sides, in an under-cosine distribution. This leads to B-rich diboride films, as long as there is no significant amount of gas scattering of the sputtered species

\* Corresponding authors.

E-mail addresses: [nhellgren@messiah.edu](mailto:nhellgren@messiah.edu) (N. Hellgren), [johanna.rosen@liu.se](mailto:johanna.rosen@liu.se) (J. Rosen).

<sup>1</sup> Present address: Department of Physics, Penn State University, State College, PA 16801, USA.

<sup>2</sup> Present address: EMPA, Swiss Federal Laboratories for Materials Science and Technology, Laboratory for Mechanics of Materials and Nanostructures, 3602 Thun, Switzerland.

<https://doi.org/10.1016/j.surfcoat.2022.128110>

Received 10 November 2021; Received in revised form 27 December 2021; Accepted 8 January 2022

Available online 14 January 2022

0257-8972/© 2022 The Authors. Published by Elsevier B.V. This is an open access article under the CC BY license (<http://creativecommons.org/licenses/by/4.0/>).

en route to the substrate. As the pressure increases, however, increased gas scattering of the sputtered atoms, primarily the lighter B atoms, results in a more even distribution of atoms in the gas phase, and the film stoichiometry approaches that of the target [16,19]. An increased target-to-substrate distance has a similar effect, since the scattering probability is proportional to the pressure-distance product [16,19]. Increased gas scattering, however, leads to lower average energy of the sputtered species impinging on the substrate, and consequently risk of lower density films. Petrov et al. [17] demonstrated a way to circumvent this by utilizing an external tunable magnetic field to assist the outer magnetic pole of the magnetron, and thereby steer more ions toward the substrate. Due to the lower ionization potential of Ti (6.8 eV) compared to B (8.3 eV) [20], the magnetic field has a larger effect on Ti ions, and therefore the B/Ti ratio is reduced. In addition, the increased flux of energetic ions serves to increase the film density. Thus, they were able to grow near-stoichiometric dense films using this method.

A related deposition technique is high power impact magnetron sputtering (HiPIMS). Rather than a constant magnetron power as used in DCMS, HiPIMS operates with short pulses of very high target current densities. This leads to a substantially higher degree of ionization of the sputtered species, and thereby additional ways to control the deposition flux utilizing magnetic fields. Bakhit et al. [21] used HiPIMS to grow films with B/Ti ratios ranging from 1.83 to 2.08 by varying the pulse length between 30 and 100  $\mu$ s, and the peak target current densities between 0.27 and 0.88 A/cm<sup>2</sup>. Subsequently, Hellgren et al. [19] grew films with B/Ti ranging from 1.4 to 2.4 depending on deposition parameters; lower pressures and/or high temperatures resulted in the lowest B/Ti ratios. This appears contrary to the trend for DCMS, but can be explained in a consistent way: at low pressures, the composition from DCMS is controlled by the initial ejection angles of the deposition flux, while for HiPIMS, the degree of ionization affects how the flux can be steered toward the substrate by magnetic fields, which in turn affects the film composition. At higher pressures, however, both of these effects are reduced due to increased gas scattering, which leads to film stoichiometries closer to that of the target, regardless of deposition technique.

Both overstoichiometric and understoichiometric films have been reported to primarily exhibit the TiB<sub>2</sub> crystalline structure (space group P6<sub>3</sub>/mmm), where hexagonal planes of B and Ti form a layered covalently bonded structure [5]. Mayrhofer et al. reported that in overstoichiometric films, the excess B forms a tissue phase between columnar TiB<sub>2</sub> crystallites [14]. In under-stoichiometric films grown by HiPIMS, on the other hand, planar stacking fault defects, with atomic layers where one or two B planes are missing, explain the excess Ti [4,22]. In both cases, the disruption of the crystalline structure inhibits the propagation of dislocations, and therefore resulted in extraordinary mechanical properties, including hardness values exceeding 40 GPa [4,14]. This can be compared to ~23–30 GPa, which is typically reported for stoichiometric bulk TiB<sub>2</sub> [5], and near-stoichiometric TiB<sub>x</sub> thin films [4]. While the lower hardness for stoichiometric TiB<sub>2</sub> can partly be explained by fewer crystallographic defects, in the case of thin films, a higher degree of porosity can also be a contributing factor, due to the higher deposition pressure necessary to produce these films.

Although it has been demonstrated that the B/Ti ratio can be controlled over a wide range, from over- to under-stoichiometric, to do so without having to sacrifice film density by growing at high pressures, requires specialized equipment, either in the form of a HiPIMS power supply or a tunable magnetic field in the deposition chamber. Those options might not be available in all research labs or production facilities, and therefore it is of interest to explore alternative ways to independently control the film composition.

Here, we report on a method to accurately control the TiB<sub>x</sub> film composition over a wide range, without altering important deposition parameters, such as pressure or ion energy, by co-sputtering from a TiB<sub>2</sub> and Ti target. By keeping the TiB<sub>2</sub> target power constant at 250 W and increasing the Ti target power from 0 to 100 W, we were able to grow films with B/Ti ratios ranging from 2.8 to 1.2. After initial analysis of

microstructure, electrical and mechanical properties, the films were annealed in vacuum at 1100 °C for 2 h, and then reanalyzed with the same techniques. This offers a direct way to compare TiB<sub>x</sub> films of various compositions, without the influence from changing deposition conditions that affect the energy distribution of the deposition flux.

## 2. Experimental procedure

TiB<sub>x</sub> films were deposited by dc magnetron co-sputtering from TiB<sub>2</sub> and Ti targets (both 99.99% pure, Stanford Advanced Materials) in a high vacuum system with a base pressure  $<1 \times 10^{-7}$  Torr ( $1.3 \times 10^{-5}$  Pa). The 76 mm-diameter targets were mounted on two magnetically decoupled magnetron cathodes, positioned at angle of 25° and distance of 15 cm from the center of the rotating substrate table, as illustrated in Fig. 1. The process gas was pure Ar (99.9999%) at a pressure of 2.2 mTorr (0.3 Pa), introduced into the deposition chamber via a mass-flow controller. The substrates were Si(001) and Al<sub>2</sub>O<sub>3</sub>(0001) wafers, which were ultrasonically cleaned for 10 min in acetone, followed by 10 min in isopropyl alcohol, then dried by N<sub>2</sub>. A ~50-nm-thick Ti buffer layer was deposited on the Al<sub>2</sub>O<sub>3</sub> substrates in order to make the surface conducting, as a negative substrate bias of -100 V was applied during all TiB<sub>x</sub> film depositions to promote crystallinity. The substrates were mounted by clips onto the substrate holder and loaded into the deposition chamber and were then heated to a deposition temperature of 450 °C, as monitored by a calibrated thermocouple in the substrate holder. The power on the TiB<sub>2</sub> cathode was kept constant at  $P_{\text{TiB}_2} = 250$  W for all depositions, which corresponded to target currents and voltage of ~0.6 A and 415 V, respectively. In order to vary the film Ti concentration, the Ti power was increased from  $P_{\text{Ti}} = 0$  W to 100 W, in 25 W increments. At  $P_{\text{Ti}} = 100$  W, the target current reached 0.26 A and the target voltage was 380 V. All films were deposited for 100 min, which resulted in film thicknesses ranging from 390 to 620 nm, as  $P_{\text{Ti}}$  increased from 0 W to 100 W.

Film composition was measured by time-of-flight elastic recoil detection analysis (ToF-ERDA) and Rutherford Backscattering Spectrometry (RBS). ERDA was used to obtain elemental distributions of light elements on the samples, e.g., H, N, O, and C contaminations as well as TiB<sub>x</sub> stoichiometry. Atomic area density, as well as more accurate concentrations of Ti and B was obtained by RBS combined with ToF-

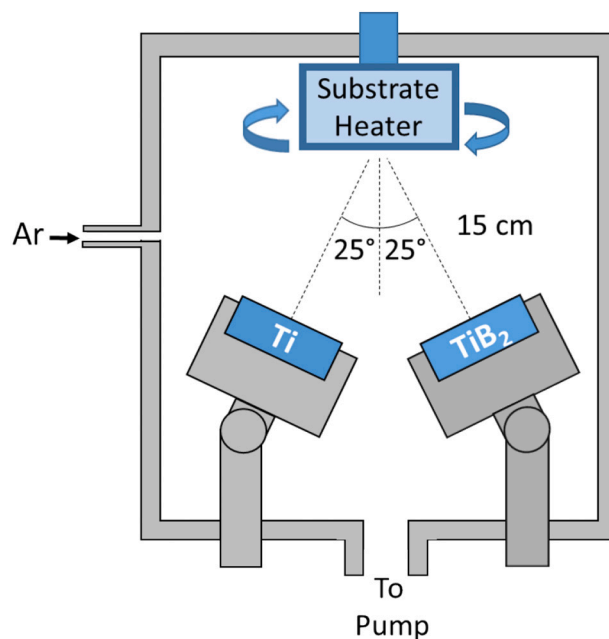


Fig. 1. Schematic drawing of the dual magnetron sputtering system used for co-sputtering of TiB<sub>x</sub> films in this study.

ERDA. Both techniques employ ion beams provided by the 5 MV 15SDH-2 tandem accelerator at the Tandem Laboratory at Uppsala University. ToF-ERDA experiments were performed with a 36 MeV  $^{127}\text{I}^{8+}$  beam with a recoil angle of  $45^\circ$  and incidence angle of  $67.5^\circ$  with the surface normal. RBS experiments were performed with a 2 MeV  $^4\text{He}^+$  beam with scattering angle of  $170^\circ$ . The incidence angle was  $5^\circ$  with respect to the surface normal and a wiggling algorithm was used during acquisition to perform series of random small angle tilts on the sample, in order to minimize channeling effects on the crystalline substrate.

Film thickness and morphology were analyzed on cleaved samples with a LEO 1550 Gemini FEG scanning electron microscope (SEM), operating with an acceleration voltage between 3 and 10 keV. The film thickness values were used for determining deposition rate, film density, and electrical resistivity.

The structure and texture were analyzed by x-ray diffraction (XRD)  $\theta$ – $2\theta$  scans, using a PANalytical X'Pert Pro powder diffractometer with  $\text{Cu } K_\alpha$  radiation ( $\lambda = 1.54 \text{ \AA}$ ). The optics utilized for these measurements were a graded Bragg–Brentano HD with  $1/2^\circ$  divergent and  $1/2^\circ$  anti-scatter slits for the incident beam side, and a 5 mm antiscatter slit together with a Soller slit for the diffracted beam side. A  $20$ – $80^\circ$  continuous scan was performed on the sample using a step size of  $0.05^\circ$  with a 10 s time per step.

High-resolution scanning transmission electron microscopy (HRSTEM) imaging, electron energy loss spectroscopy (EELS) and selective area electron diffraction (SAED) were used to determine the microstructure, and to further verify the elemental distribution and crystallographic relations of the films. Microscopy was performed using the Linköping double corrected FEI Titan<sup>3</sup> 60–300 operated at 300 kV. STEM high angle annular dark field (STEM-HAADF) imaging was performed using a  $21.5 \text{ mrad}$  convergence semi-angle, which provided sub-Ångström resolution probes with  $\sim 60 \text{ pA}$  beam current and using an angular detection range of  $46$ – $200 \text{ mrad}$ . EELS spectrum images of  $50 \times 50$  pixels were acquired using the Gatan GIF Quantum ERS post-column imaging filter with a  $0.25 \text{ eV/channel}$  energy dispersion,  $0.2 \text{ s}$  pixel dwell time and a collection semi-angle of  $55 \text{ mrad}$ . Elemental B, Ti and O distribution maps were extracted from the spectrum images using a power law background subtraction, and choosing characteristic edges B–K ( $188$ – $208 \text{ eV}$ ), Ti– $L_{23}$  ( $455$ – $470 \text{ eV}$ ) and O–K ( $532$ – $570 \text{ eV}$ ) energy loss integration windows. Plan-view TEM samples were prepared by a combined approach, which included mechanical cutting, cleaving, and polishing to a few hundred  $\mu\text{m}$  thickness from the substrate side. The samples were then fixed to the Cu grid and final milling was performed by focused ion beam, employing a Carl Zeiss Cross-Beam 1540 EsB system [23].

X-ray photoelectron spectroscopy (XPS) analysis was done using a Kratos Ultra DLD instrument (Kratos Analytical, UK), equipped with a monochromatic  $\text{Al } K_\alpha$  source ( $h\nu = 1486.7 \text{ eV}$ ) and a concentric hemispherical analyzer. Samples were analyzed both as-deposited, after exposure to atmosphere for several days, as well as after  $\text{Ar}^+$  sputter cleaning to remove surface oxides and contamination. The sputter cleaning procedure used consisted of (I) etching for 2 min using a  $4 \text{ keV}$   $\text{Ar}^+$  ion beam incident at an angle of  $70^\circ$  relative to the surface normal, followed by (II) 5 min at  $0.5 \text{ keV}$ . The first (I) step has been verified to remove most surface oxides and contaminants, while the second (II) step provides a gentler etch, intended to reduce the amount of surface damage induced by the first step [24,25]. High-resolution core level spectra were obtained using a pass energy of  $20 \text{ eV}$ , which results in the full width at half maximum of  $0.55 \text{ eV}$  for the  $\text{Ag } 3d_{5/2}$  peak from the reference sputter-cleaned Ag sample. All spectra were collected at normal emission angle, and without any ion or electron charge neutralization applied. Spectra were charge corrected by setting the B 1s peak component corresponding to  $\text{TiB}_2$  to  $187.70 \text{ eV}$ , as explained in detail in Ref. [26].

Mechanical properties of the films were studied with the aid of a Hysitron TI 950 nanoindenter system. To investigate the indentation hardness,  $H$ , and combined elastic modulus of the contacting bodies,  $E^*$ ,

every sample was subjected to 90 indentations with a Berkovich diamond tip within the load range of  $0.1$ – $13 \text{ mN}$ . The  $H$  and  $E^*$  values were obtained by evaluating the load–displacement curves by means of the Oliver and Pharr method [27]. Subsequently, the elastic modulus of the films,  $E$ , was calculated assuming a Poisson's ratio,  $\nu$ , of  $0.15$  [28,29]. Given the impact of the stoichiometry on the elastic constants of  $\text{TiB}_x$ , the upper and lower limits of  $E$  were calculated for a Poisson's ratios of  $0.1$  and  $0.3$ , respectively [30,31]. After plotting  $H$  and  $E$  values as a function of penetration depth, only  $H$  values from a fully developed plastic zone and yet unaffected by the substrate were considered film-only hardness, while a smooth curve was fitted to the  $E$  values and subsequently extrapolated back to zero depth to obtain film-only elastic modulus.

Electric resistivity of films deposited on  $\text{Al}_2\text{O}_3$  substrates was measured at room temperature by a four point probe (Jandel Engineering Ltd., UK). Since the measured resistivity is a combination of that of the  $\text{TiB}_x$  film and Ti buffer layer, the resistivity of the  $\text{TiB}_x$  layer alone was obtained using the following equation [32]:

$$\rho_{\text{eff}} = (t_{\text{Ti}} + t_{\text{TiB}_x}) \frac{\rho_{\text{Ti}} \rho_{\text{TiB}_x}}{t_{\text{Ti}} \rho_{\text{TiB}_x} + t_{\text{TiB}_x} \rho_{\text{Ti}}} \quad (1)$$

where  $\rho$  is the electrical resistivity of the material and  $t$  is the film thickness.

After initial analysis of the as-deposited samples, films deposited on  $\text{Al}_2\text{O}_3$  substrates were annealed at  $1100^\circ\text{C}$  for 2 h in vacuum ( $p \leq 5 \times 10^{-8} \text{ Torr}$ ,  $6.7 \times 10^{-6} \text{ Pa}$ ), then reanalyzed with the same techniques, in order to monitor changes to film crystallinity and properties. The temperature was ramped up at  $\sim 50^\circ\text{C/min}$ , and the samples were allowed to fully cool to room temperature before removing from the vacuum chamber.

### 3. Results and discussion

Fig. 2 shows the resulting B/Ti ratio of the films, both as-deposited and after annealing. The as-deposited film grown from the  $\text{TiB}_2$  target only ( $P_{\text{Ti}} = 0 \text{ W}$ ) is over-stoichiometric with a B/Ti ratio of  $2.8 \pm 0.2$ , as is typical for magnetron sputtered  $\text{TiB}_x$  films at low pressure [3,17–19]. The error bars correspond to random variation in the concentration depth profiles from ToF-ERDA, as well as, for several films, a slight concentration gradient, with lower B/Ti close to the surface. As  $P_{\text{Ti}}$  increases, the B/Ti ratio decreases in a close to linear fashion, and for  $P_{\text{Ti}} = 100 \text{ W}$  results in a B/Ti  $\approx 1.2 \pm 0.1$ . The linear trend shows that the

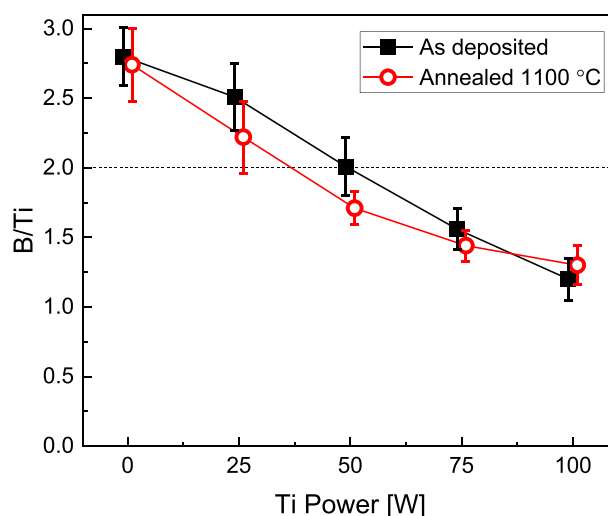


Fig. 2. B/Ti ratio of the co-sputtered  $\text{TiB}_x$  films as a function of power on the Ti target,  $P_{\text{Ti}}$ , before and after vacuum annealing at  $1100^\circ\text{C}$  for 2 h. The horizontal line represents the composition of stoichiometric  $\text{TiB}_2$ .

composition can be easily and accurately controlled over a wide range. After annealing, the B/Ti ratio is reduced slightly (by  $\sim 0.1$ – $0.3$ ) for the films grown with  $P_{Ti} \leq 50$  W, but increases by  $\sim 0.1$  for the most Ti-rich film grown with  $P_{Ti} = 100$  W. The major reason for this trend is likely diffusion between the  $TiB_x$  film and the Ti buffer layer. If that was the only reason, however, the compositions should presumably always go toward stoichiometry; in under-stoichiometric films, Ti from the buffer layer diffuses into the film, while B from the film would diffuse into the buffer layer for the over-stoichiometric films. Since this is not the case for the films grown with  $P_{Ti} = 50$  and  $75$  W, some other effect must also be in play. We propose that the reason is evaporation of  $B_2O_3$  (g) during annealing [33–35]. About 2.5–4 at.% of oxygen is detected in the bulk of the as-deposited film, and significantly more ( $\sim 30$ – $50$  at.% according to XPS) on the surface, due to post-deposition exposure to atmosphere. Oxygen can react with boron in grain boundaries to form  $B_2O_3$ , which desorbs at elevated temperatures [33–35]. This effect will obviously be more dominant for B-rich films, but can lower the B/Ti for all compositions. Other factors that can influence how the composition is affected by annealing are film density, microstructure, as well as thickness of film and buffer layer, and they all may contribute to the observed trend.

Fig. 3(a) shows the film thickness and deposition rate as a function of  $P_{Ti}$ , both for as-deposited films and after annealing. As expected, the film thickness in general increases with increasing  $P_{Ti}$ . The exception is when  $P_{Ti}$  increases from 25 to 50 W, where the film thickness and deposition rate essentially stay constant, in spite of an increased deposition flux of Ti. This apparent inconsistency can be explained by an increased film density, as shown in Fig. 3(b). The under-stoichiometric film grown with  $P_{Ti} \leq 25$  W have a density of  $\sim 3.3 \pm 0.4$  g/cm<sup>3</sup>, but it increases to  $\sim 3.9 \pm 0.4$  g/cm<sup>3</sup> for the over-stoichiometric film grown with  $P_{Ti} \geq 50$  W. All densities are significantly higher than those of bulk B ( $2.34$  g/cm<sup>3</sup> [36]), but lower than bulk  $TiB_2$  ( $4.52$  g/cm<sup>3</sup> [5]) and Ti ( $4.51$  g/cm<sup>3</sup> [36]). They also fall below those reported by Thörnberg et al. ( $4.0$ – $4.2$  g/cm<sup>3</sup> for DCMS films, and  $4.3$  g/cm<sup>3</sup> for films grown by HIPIMS [4]), suggesting that the present films have more porous microstructures as discussed below. This is likely a consequence of the comparatively large target-to-substrate distance (15 cm), which leads to a relatively low ion flux at the substrate, since the magnetic field strength is decaying with distance from the magnetron.

From Fig. 3(a) we notice that the thickness did not change significantly with annealing. However, the variation in the thickness measured by SEM at multiple locations along the cross sections increased considerably, which is reflected in the larger error bars. Some of this effect can be found in Fig. 4, which shows cross-sectional SEM micrographs of films grown with  $P_{Ti} = 0, 50$  and  $100$  W, before and after annealing. The as-deposited films show tendencies of columnar growth and smooth surfaces, which is frequently observed for magnetron sputtered  $TiB_x$

films [2–4,18]. After annealing, however, the films appear to become less columnar, with increasing surface roughness, and increased long-range thickness variations. This indicates that material is redistributed within the films, presumably by diffusion along the surface as well as in and across grain boundaries, and likely driven by concentration gradients and stress relief.

Fig. 5 shows XRD diffractograms of  $TiB_x$  films grown with  $P_{Ti} = 0, 50$ , and  $100$  W before and after annealing. The as-deposited films grown with  $P_{Ti} \geq 75$  W for the most part are amorphous (at least X-ray amorphous), with no peaks corresponding to crystallites in the film. Films grown with  $P_{Ti} \leq 50$  W, on the other hand, show  $TiB_2$  ( $10\bar{1}0$ ) and ( $10\bar{1}1$ ) peaks, indicating polycrystalline structure with a preferred texture. After annealing, those peaks grow in intensity, suggesting a larger fraction of the film is crystalline. However, the peak widths do not change significantly, indicating that the average crystal grain size remains largely unchanged (a larger grain size would manifest itself by narrower peaks). Since the annealing temperature is less than half of the melting temperature of  $TiB_2$  ( $\sim 3225$  °C [5]), only surface diffusion should be possible. However, based on Fig. 3(b), at least part of the amorphous matrix is under-dense, which makes diffusion feasible. Thus, some of the amorphous matrix is transformed into crystallites, but the average grain size is still small. An estimate using the Scherrer equation [37] suggests crystallite sizes of 15–20 nm.

The initially amorphous films grown with  $P_{Ti} \geq 75$  W develop several new peaks upon annealing, most noticeable the (0001), ( $10\bar{1}0$ ), ( $10\bar{1}1$ ), and (0002) peaks of  $TiB_2$ , with (0001) and (0002) being the largest. No other peaks corresponding to known allotropes of titanium boride are observed, showing that  $TiB_2$  crystallites are embedded in an amorphous matrix, which accommodates the off-stoichiometric constituents. Additional peaks at  $36.6^\circ$  and  $42.6^\circ$  also emerge after annealing of the Ti-rich films. As shown below, these peaks do not originate from the film, but presumably from the film-substrate interface. The substrates were coated with a Ti buffer layer, which does not exhibit any XRD peaks prior to annealing. In the case of the Ti-deficient films grown with  $P_{Ti} \leq 50$  W, rather than forming Ti crystallites, it appears more favorable for the interface Ti to migrate into the bottom portion of the  $TiB_x$  film and bond to surplus B. For the Ti rich films grown with a higher  $P_{Ti}$ , however, that is not feasible. Instead, Ti remains in the buffer layer, possibly reacting with the  $Al_2O_3$  substrate to form various Ti-Al-O crystallites at the interface, which are manifested in the additional peaks.

Fig. 6 shows plan-view STEM images of  $TiB_x$  films grown with  $P_{Ti} = 0, 50$ , and  $100$  W after annealing. It reveals significant differences in the microstructure depending on B/Ti ratio: The B-rich film grown with  $P_{Ti} = 0$  W (Fig. 6(a)) shows a nanogranular, or possibly nanocolumnar,

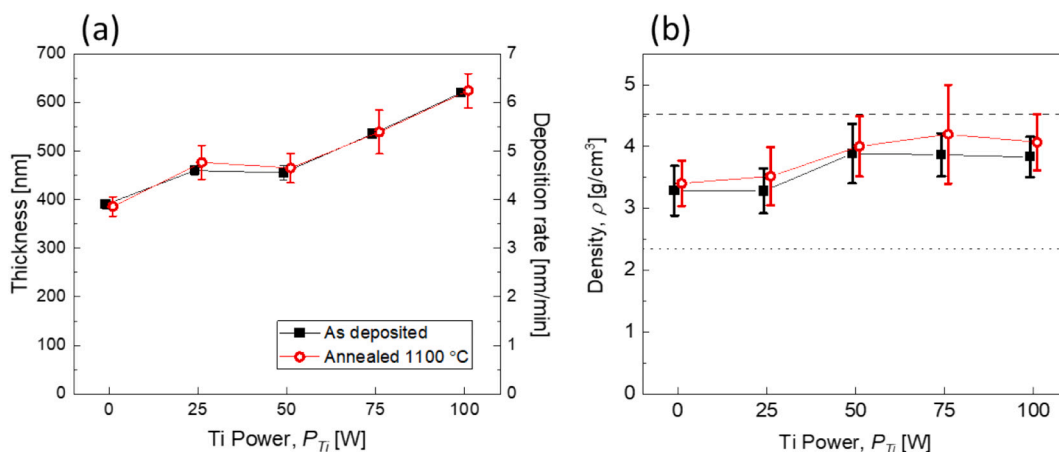


Fig. 3. (a) Film thickness and deposition rate, and (b) density of the co-sputtered  $TiB_x$  films as a function of  $P_{Ti}$ , before and after vacuum annealing at  $1100$  °C for 2 h. The dashed horizontal line in (b) represents the density of bulk  $TiB_2$  ( $4.52$  g/cm<sup>3</sup>) and Ti ( $4.51$  g/cm<sup>3</sup>), and the dotted line the density of bulk B ( $2.34$  g/cm<sup>3</sup>).



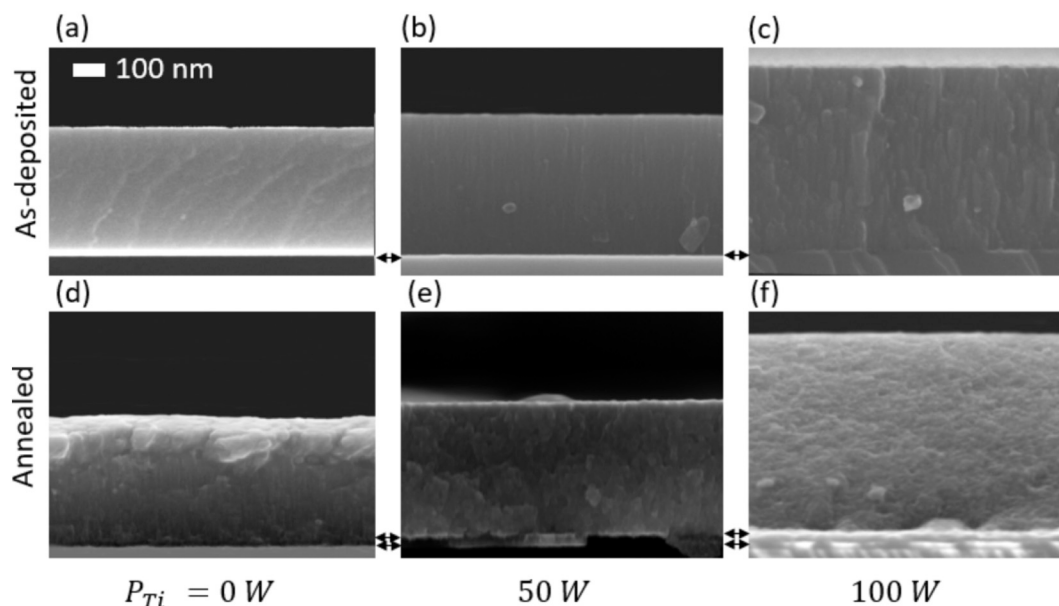


Fig. 4. Cross-sectional SEM micrographs of the co-sputtered  $\text{TiB}_x$  films grown with  $P_{\text{Ti}} = 0, 50$ , and  $100$  W before (on Si substrates) and after ( $\text{Al}_2\text{O}_3$  substrates) vacuum annealing at  $1100^\circ\text{C}$  for 2 h. The scale is the same for all images. The arrows indicate the interfaces between substrate, buffer layer and  $\text{TiB}_x$  film.

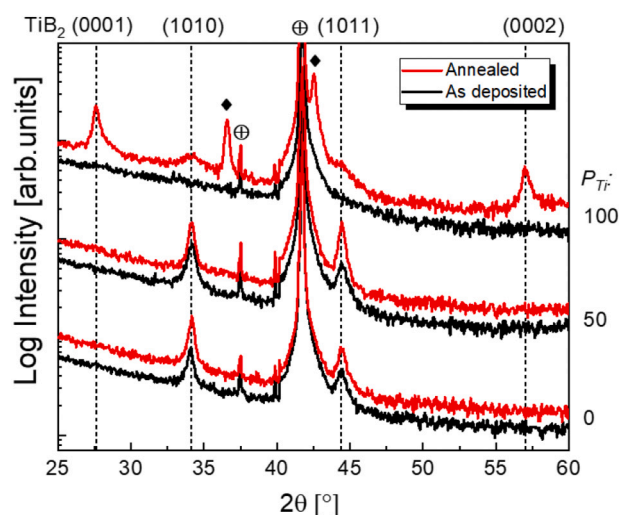


Fig. 5. X-ray 0-2 $\theta$  diffractograms from the co-sputtered  $\text{TiB}_x$  films grown with  $P_{\text{Ti}} = 0$  to  $100$  W, before (black/lower lines) and after (red/upper lines) vacuum annealing at  $1100^\circ\text{C}$  for 2 h. The graphs have been offset for better visibility.  $\text{Al}_2\text{O}_3$  substrate peaks are marked with  $\oplus$ , and interface/buffer layer peaks with  $\blacklozenge$ . (For interpretation of the references to colour in this figure legend, the reader is referred to the web version of this article.)

structure with rather smooth crystallites of typical size 5–15 nm, which is in reasonable agreement with the estimate from XRD. EELS  $\text{Ti-L}_{23}$  and B-K-edge maps (inset in Fig. 6(a)) show a fairly uniform distribution of B. The Ti distribution, on the other hand, exhibits more variation, with very low intensity between the grains. Together with the XRD data, this indicates that the microstructure consists of stoichiometric  $\text{TiB}_2$  crystallites, with surplus B located in the grain boundaries. This is consistent with what has been observed by other researchers [4,14,38,39]. Regions of low B intensity (dark) also correlate with regions of low Ti intensity, showing that voids are present. The diameter of these voids ranges between 5 and 15 nm, i.e., the same, or slightly smaller, size as the typical crystallites. It should be noted that not all dark regions in the Ti map correspond to voids, but there are also B-rich/Ti-deficient regions dispersed in the film. The contrast in STEM imaging depends largely on

grain orientation relative to the electron beam, and it is therefore difficult to detect density variations from STEM alone.

The near-stoichiometric film grown with  $P_{\text{Ti}} = 50$  W (Fig. 6(b)) shows a connected network of elongated crystallites, up to  $\sim 50$  nm in length and approximately 10–20 nm wide. Relatively large voids are present between the crystallites, but the overall number density of voids appears reduced compared to the films grown with  $P_{\text{Ti}} = 0$  W, which explains the slightly higher film density (see Fig. 3(b)). The O-K EELS map show that oxygen migrates into the film via voids and grain boundaries, but very little O is detected inside the  $\text{TiB}_2$  grains. As  $P_{\text{Ti}}$  increases to  $100$  W (Fig. 6(c)), the film becomes even more continuous, and the crystallite size decreases. The void density is significantly reduced compared to the other samples, which is consistent with a higher mass density (Fig. 3(b)). The EELS maps reveal a uniform distribution of Ti, but a varying B concentration, i.e., similar to the B-rich sample, but with B and Ti reversed. This is in contrast to under-stoichiometric samples grown by HiPIMS, where the B-deficiencies are accounted for by islands of planar defects of missing B-layers [4,22]. Thus, the microstructure is not just a function of composition, but also of deposition technique, and more specifically, the energy and flux imparted to the film during growth. The O distribution is anti-correlated to B, which shows that any O that migrates into the film is attracted to the surplus Ti.

The inserts in Fig. 6 show SAED patterns from the three films. All diffraction spots form more or less continuous rings, indicating that the crystallites in all samples are randomly oriented. Brighter points along the rings suggest that some crystallites are larger, but no preferred orientation is evident in the analyzed volumes. By integrating the intensities in concentric rings around the central beam, we can plot the relative intensities of the diffractions vs. reciprocal distance, as shown in Fig. 7. Overall, the pattern is similar to XRD (Fig. 5), although the relative intensities of the different peaks vary somewhat. For instance, for the film grown at  $P_{\text{Ti}} = 100$  W, the (1010) peak is dominating the SAED, whereas the (0001) and (0002) are the largest in the XRD pattern. This can be explained by the measurement geometry; in XRD 0-2 $\theta$  scans, planes parallel to the film surface are detected, whereas in SAED, the diffraction is originating from planes that are oriented parallel to the electron beam direction, i.e., perpendicular to the film surface in this case. The fact that all diffraction peaks are present in the SAED patterns, while only select planes are seen by XRD, indicate that the films have a

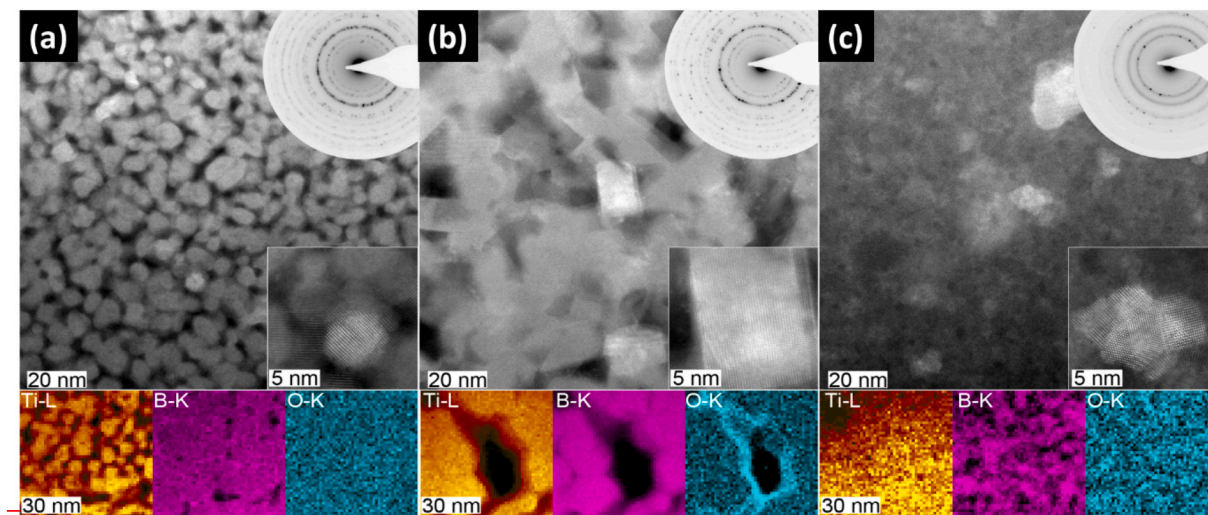


**Fig. 6.** Plan-view STEM micrographs of the co-sputtered  $\text{TiB}_x$  films grown with  $P_{\text{Ti}} = 0$  (a), 50 (b), and 100 W (c) after vacuum annealing at 1100 °C for 2 h. The inserts show higher resolution images, SAED patterns, as well as Ti-L<sub>2,3</sub>, B-K and O-K-edge EELS elemental distribution maps. The SAED diffraction rings are indexed in Fig. 7.

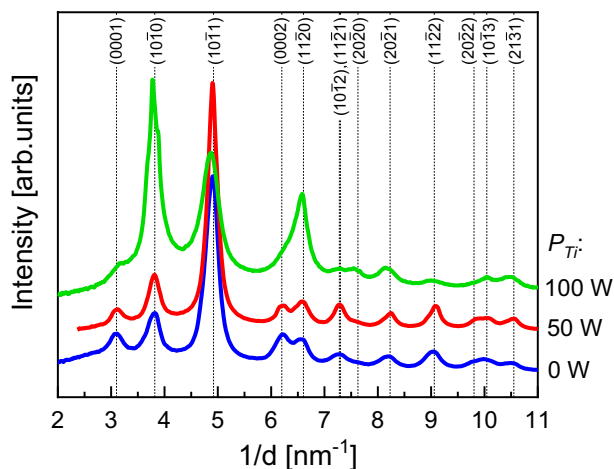


**Fig. 7.** Integrated intensities vs. radius (i.e., reciprocal distance) from SAED patterns shown in Fig. 6, for the co-sputtered  $\text{TiB}_x$  films grown at  $P_{\text{Ti}} = 0$  W, 50 W, and 100 W, after vacuum annealing at 1100 °C for 2 h. All peaks can be assigned to hexagonal  $\text{TiB}_2$ , as indicated.

preferred orientation in the growth direction, whereas the in-plane rotation of the crystallites is random. Furthermore, since all SAED peaks can be attributed to  $\text{TiB}_2$  in the hexagonal P6/mmm structure, the additional, unassigned, peaks seen in XRD would not originate from the films themselves, but most likely from the film-substrate interface.

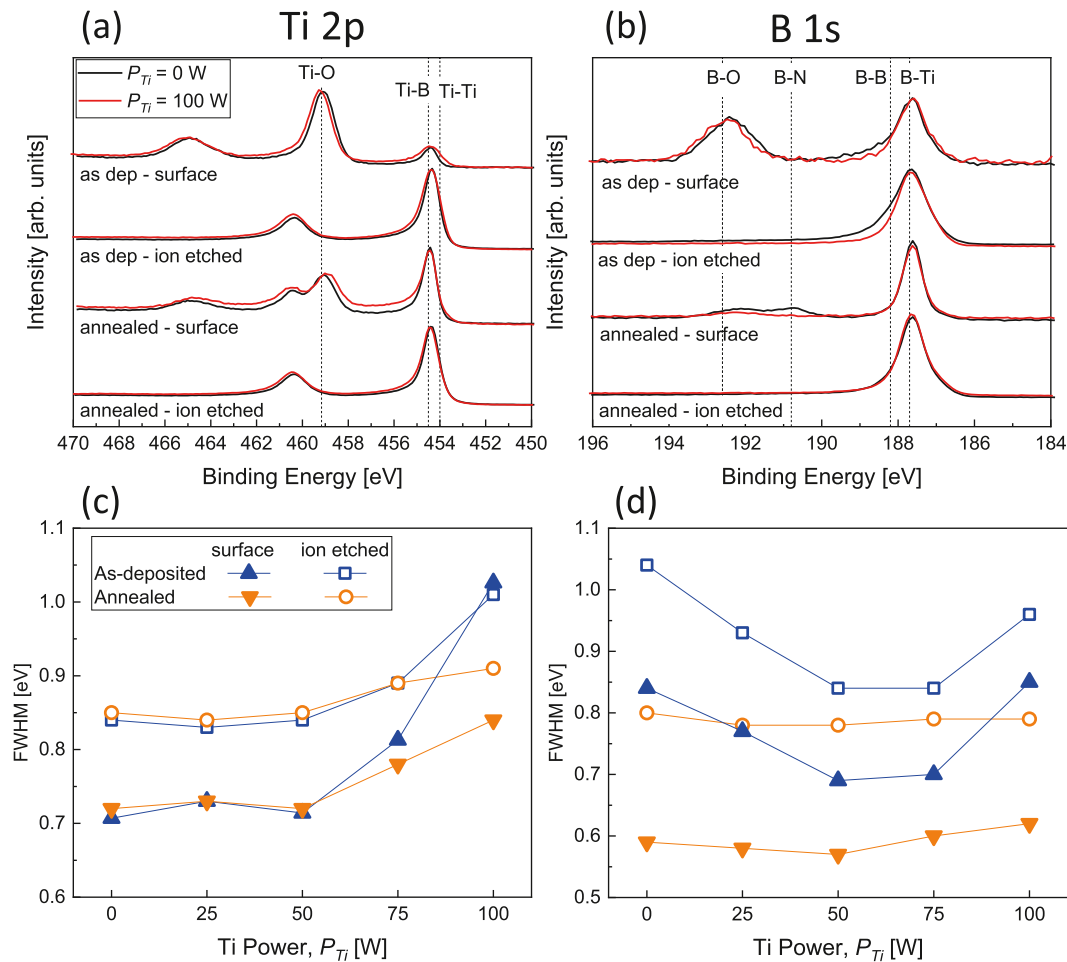
It can be noticed that the  $(10\bar{1}0)$  peak for the film grown at  $P_{\text{Ti}} = 100$  W appears to consist of two, maybe three, sub-peaks. Similarly, other peaks, most noticeably the  $(10\bar{1}1)$  peak, are wider for this sample compared to the other. This is due to some of the brighter spots in the SAED pattern (originating from larger crystallites) being offset slightly from the fainter continuous diffraction ring. This variation in lattice parameters may be explained by structural defects and internal stress in this Ti-rich sample.

Fig. 8 (a) and (b) shows XPS Ti 2p and B 1s XPS spectra, respectively, for the films grown at  $P_{\text{Ti}} = 0$  and 100 W, before and after vacuum annealing, as well as before and after ion etching (effectively sputter-cleaning). The spectra show the characteristic peaks of  $\text{TiB}_2$  (B1s at 187.7 eV, Ti 2p<sub>3/2</sub> at 454.5 eV, and Ti 2p<sub>1/2</sub> at 460.5 eV), as well as oxide peaks on the as-deposited samples ( $\text{B}_2\text{O}_3$  at 192.6 eV and  $\text{TiO}_2$  at 459.2

and 465.0 eV), in agreement with previous reports [26]. After annealing, the oxide-related peaks are not as intense as on the as-deposited samples, especially the  $\text{B}_2\text{O}_3$  peaks are almost entirely removed, while the  $\text{TiO}_2$  peak is smaller than on the as-deposited sample, but still prominent. This can be explained by  $\text{B}_2\text{O}_3$  sublimating off the surface during annealing due to its high vapor pressure [33]. Furthermore, any residual hydrogen or water vapor would promote the formation of boric acid ( $\text{H}_3\text{BO}_3$ ), which would quickly evaporate at elevated temperatures [33–35].  $\text{TiO}_2$  is more stable, which explains that it is the major oxide phase left after annealing. On the over-stoichiometric films grown at  $P_{\text{Ti}} = 0$  and 25 W (not shown in Fig. 8), a small peak at ~190.7 eV indicates that some boron, left unsaturated after annealing, reacts with nitrogen. This is most likely occurring when the load-lock is vented with  $\text{N}_2$ , before the films are exposed to oxygen in the atmosphere. In all cases, any residual surface contaminants are readily removed by ion etching.

We have recently demonstrated [26] that the main Ti 2p and B 1s peaks can be deconvoluted into components corresponding to pure  $\text{TiB}_2$  (454.5 eV for Ti 2p<sub>3/2</sub>, and 187.7 eV for B 1s, respectively), and components for the surplus elements in off-stoichiometric films, namely Ti-Ti (~454.0 eV) and B-B (~188.2 eV). Due to the ~0.5 eV energy shift between the components, the overall Ti 2p<sub>3/2</sub> peak width tend to increase with increasing Ti content, and correspondingly, the B 1s peak increase with B content [26]. The Ti 2p<sub>3/2</sub> and B 1s full width at half maximum (FWHM) of all samples, before and after annealing and ion etching, are plotted in Fig. 8(c) and (d). In all cases, ion etching results in an increase in the FWHM by ~0.1–0.2 eV. This is consistent with the results in Ref. [26], and can be explained by structural distortions due to the ion bombardment. Furthermore, the trends as a function of B/Ti ratio are also consistent with previous results for the as-deposited samples [26]. It can be noted that both the Ti 2p<sub>3/2</sub> and B 1s peaks become wider for the most Ti-rich film, grown at  $P_{\text{Ti}} = 100$  W. This, too, can be related to the increased structural disorder, apparently caused by the high Ti content, as evident from the lack of film diffraction peaks detected by XRD (Fig. 5).

After annealing, the Ti 2p<sub>3/2</sub> FWHM remains largely unchanged, with the exception for the most Ti-rich films, for which the FWHM decreases, due to the increased structural order induced by annealing (see Fig. 5). The FWHM of the B 1s peak after annealing does not vary significantly depending on growth condition. The overall width, on the other hand, is considerably lower than before annealing, indicating no significant amount of B–B bonds, and therefore very little surplus B, is detected by XPS even for the over-stoichiometric films. This can likely be



**Fig. 8.** Ti 2p (a) and B 1s (b) spectra of the co-sputtered TiB<sub>x</sub> films grown at  $P_{Ti} = 0$  and  $100$  W, before and after vacuum annealing to  $1100$  °C for  $2$  h, as well as before and after ion etching. All spectra have been normalized for easier comparison. The full width at half maximum (FWHM) of the Ti 2p<sub>3/2</sub> (c) and B 1s (d) peaks corresponding to TiB<sub>2</sub> (including Ti-Ti and B-B components), vs.  $P_{Ti}$ , before and after vacuum annealing, as well as before and after ion etching. In (a), the Ti 2p<sub>3/2</sub> components are labelled. The corresponding Ti 2p<sub>1/2</sub> components are seen at  $\sim 5.5$ – $6$  eV higher binding energies.

explained by preferential desorption of B, in the form of B<sub>2</sub>O<sub>3</sub> and H<sub>3</sub>BO<sub>3</sub> during annealing, leaving a B-depleted surface layer. There is, however, still a B surplus in the sub-surface region, as evident from the ERDA composition.

The electrical resistivity,  $\rho$ , of the as-deposited and annealed films is shown in Fig. 9. Note that the film grown at  $P_{Ti} = 25$  W was delaminating and therefore did not give reproducible and reliable values. It is therefore excluded henceforth. For the as-deposited films, the film grown with  $P_{Ti} = 0$  W has the highest resistivity ( $\sim 690$   $\mu\Omega\text{cm}$ ), while the films grown with  $P_{Ti} \geq 50$  W exhibit about half that value ( $\sim 300$ – $350$   $\mu\Omega\text{cm}$ ). This can be explained partly by a higher metal content, but more importantly, a more connected network with fewer voids. This effect is even more pronounced after annealing, when all values drop by  $100$ – $200$   $\mu\Omega\text{cm}$ . The lowest resistivity,  $122$   $\mu\Omega\text{cm}$ , is obtained for the near-stoichiometric film grown with  $P_{Ti} = 50$  W. These values can be compared to reported values for bulk ( $6.6$ – $38$   $\mu\Omega\text{cm}$  [6,40]) and thin film ( $133$ – $413$   $\mu\Omega\text{cm}$  [4,41,42]) TiB<sub>2</sub>. Both Shutou et al. [41] and Todorović et al. [42] reported reduced resistivity after annealing. Shutou et al. annealed RF magnetron sputtered films with as-deposited resistivities of  $239$ – $323$   $\mu\Omega\text{cm}$  to  $600$  °C, and reported a reduction to  $\sim 150$ – $300$   $\mu\Omega\text{cm}$ , depending on deposition condition [41]. Todorović et al. saw a sudden drop in the resistivity of e-beam-deposited film from over  $200$   $\mu\Omega\text{cm}$  to below  $20$   $\mu\Omega\text{cm}$  when annealing above  $1000$  °C, and a minimum value of  $16$   $\mu\Omega\text{cm}$  after  $1200$  °C [42]. This was explained by grain growth through polycrystalline recrystallization, and increased film density.

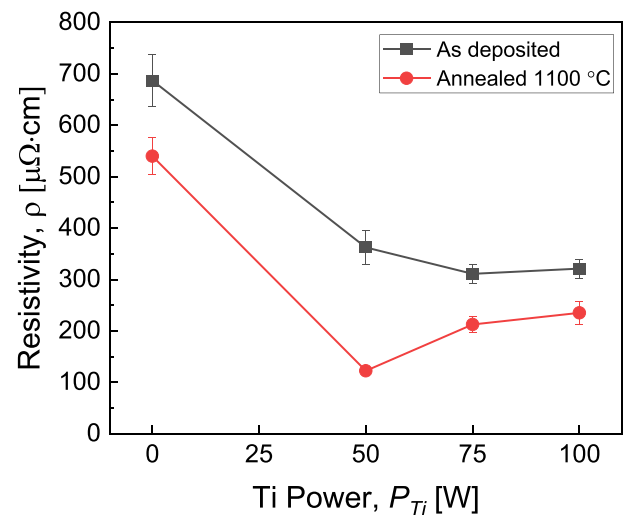


**Fig. 9.** Electric resistivity,  $\rho$ , of the co-sputtered TiB<sub>x</sub> films grown with  $P_{Ti} = 0$  to  $100$  W, before and after vacuum annealing at  $1100$  °C for  $2$  h. The error bar for the  $50$  W sample after annealing is approximately the same size as the marker.



While the response to annealing is similar in our case, neither the density nor grain size changes significantly upon annealing. However, a higher portion of the material is transformed from amorphous to crystalline, and therefore a more connected polycrystalline network is formed. The fact that the near-stoichiometric film shows the lowest resistivity after annealing further confirms that the off-stoichiometric grain boundaries are major contributors to the overall resistivity. This is likely enhanced by the fact that Ti has a higher affinity for oxidation compared to the stoichiometric portions of the film (see Fig. 6(c)). This results in an increased resistivity for the films grown  $P_{Ti} \geq 75$  W, in spite of higher metal content. Although the films grown at  $P_{Ti} = 50$  W exhibit rather large voids and oxidized grain boundaries (see Fig. 6(b)), the overall oxidation level low ( $\sim 2$  at.%) and the grain boundaries are thin between the crystalline  $TiB_2$  crystallites, which results in the lowest resistivity.

Fig. 10 shows the nanoindentation hardness ( $H$ ) and elastic modulus ( $E$ ) for the as-deposited and annealed films as a function of  $P_{Ti}$ . Again the film grown with  $P_{Ti} = 25$  W has been excluded due to inconsistent results owing to delamination. The hardness (Fig. 10(a)) of the as-deposited films decreases slightly, from  $\sim 29$  to  $\sim 26$  GPa as  $P_{Ti}$  increases from 0 to 100 W. After annealing the hardness decreases for films grown with  $P_{Ti} \leq 50$  W, and increases for  $P_{Ti} \geq 75$  W, and the highest value of  $\sim 32$  GPa is recorded for the most under-stoichiometric film, grown with  $P_{Ti} = 100$  W. At the same time, variation in the nanoindentation response increases, which is reflected in the significantly larger error bars after annealing. This suggests that the film structure is not uniform over large areas, which could be due to non-uniform distribution of voids, or inconsistent properties of the grain boundaries.

The elastic modulus of the as-deposited films varies from  $\sim 380$  to  $\sim 470$  GPa, with the highest value for the film grown at  $P_{Ti} = 50$  W, and decreasing for the off-stoichiometric films in both directions. After annealing, the trend is more monotonously increasing from  $\sim 400$  to  $\sim 470$  GPa as  $P_{Ti}$  increases from 0 to 100 W. While all variations are only slightly larger than the measurement uncertainties, the trends for both  $H$  and  $E$  suggest that the mechanical strength after annealing is increasing with increasing Ti concentration. This is due to the combined effect of higher film density and off-stoichiometric grain boundaries, which hamper the propagation of dislocations.

These above hardness and modulus values for the present films can be compared to Thörnberg et al., who reported  $H = 37.7 \pm 0.8$  GPa and  $E = 508 \pm 6$  GPa for DCMS-sputtered over-stoichiometric  $TiB_{2.7}$  (corresponding to our film grown with  $P_{Ti} = 0$  W), and  $H = 22.3 \pm 0.6$  GPa and  $E = 393 \pm 5$  GPa for near-stoichiometric  $TiB_{2.2}$  (similar to  $P_{Ti} = 50$  W). Thus, Thörnberg et al. showed a substantially larger difference depending on B/Ti ratio. However, those results are convoluted by the condition that a higher deposition pressure is required to get near-stoichiometric films, and those films therefore tend to be less dense. Here, the under-stoichiometric film grown with  $P_{Ti} = 0$  W has the lowest

density, but still exhibits similar mechanical response as the near-stoichiometric film grown with  $P_{Ti} = 50$  W. This shows that even when the density is factored out, the off-stoichiometric grain boundaries play a major role in promoting hard and deformation-resistant films.

#### 4. Conclusions

We have grown  $TiB_x$  films with  $1.2 \leq x \leq 2.8$  by magnetron co-sputtering from  $TiB_2$  and Ti targets in pure Ar. The film structure and properties are characterized before and after vacuum-annealing at  $1100^\circ\text{C}$  for 2 h. The film B/Ti ratio scales linearly with the Ti target power, while keeping the  $TiB_2$  target power constant. Films grown without additional Ti are over-stoichiometric (B-rich), and in general exhibit the lowest density, due to voids and an amorphous tissue phase of excess B interspersed in a microstructure of small randomly oriented  $TiB_2$  crystallites of size  $\sim 5$  to 25 nm. Films grown with  $P_{Ti} \geq 75$  W are under-stoichiometric (Ti-rich), with higher density. The as-deposited films are mostly amorphous, but crystallize upon annealing, with a preferred (0001) texture according to XRD. The grain size is similar to the over-stoichiometric films, but with fewer voids and surplus Ti in a tissue phase between grains. The near-stoichiometric films grown at  $P_{Ti} = 50$  W consist of a connected network of elongated crystallites of typical length 50 nm and 10–20 nm width, as judged from STEM imaging, with relatively large voids between. As a consequence of the compositional and structural variations, the resulting film resistivity and mechanical properties change. The electrical resistivity decreases with increasing grain size and film density. Thus, the lowest value,  $122 \mu\Omega\text{cm}$ , is observed for the near-stoichiometric film after annealing. While all films exhibit high hardness values in the 25–30 GPa range, the highest value of  $\sim 32$  GPa is obtained for the most Ti-rich film after annealing. This is due to the high density and nano-crystalline microstructure, where dislocation propagation is interrupted by the off-stoichiometric grain boundaries. The present approach offers a way to independently control the film composition and deposition pressure, which are otherwise closely linked.

#### CRediT authorship contribution statement

**Niklas Hellgren:** Investigation, Writing – original draft, Supervision, Project administration. **Alexander Sredenshek:** Investigation, Writing – review & editing. **Andrejs Petruins:** Investigation, Writing – review & editing. **Justinas Palisaitis:** Investigation, Writing – review & editing. **Fedor F. Klimashin:** Investigation, Writing – review & editing. **Mauricio A. Sortica:** Investigation, Writing – review & editing. **Lars Hultman:** Writing – review & editing, Funding acquisition. **Per O.Å. Persson:** Investigation, Writing – review & editing. **Johanna Rosen:** Supervision, Resources, Project administration, Funding acquisition,

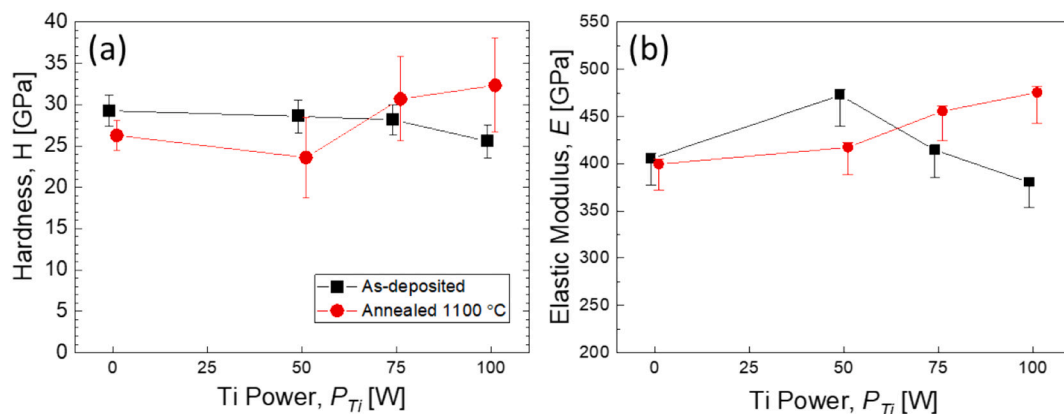


Fig. 10. (a) Hardness,  $H$ , and (b) elastic modulus,  $E$ , of the co-sputtered  $TiB_x$  films grown with  $P_{Ti} = 0$  to 100 W, before and after vacuum annealing at  $1100^\circ\text{C}$  for 2 h.



Writing – review & editing.

## Declaration of competing interest

The authors declare that they have no known competing financial interests or personal relationships that could have appeared to influence the work reported in this paper.

## Acknowledgements

Financial support from the Knut and Alice Wallenberg (KAW) Foundation, Project grant number KAW 2015.0043 and support of the electron microscopy laboratory in Linköping. Swedish Foundation for Strategic Research (SSF), contracts RIF14-0053, RIF 14-0074 and VR-RFI (contract #2017-00646.9) are greatly appreciated.

## References

- [1] M. Berger, M. Larsson, S. Hogmark, Evaluation of magnetron-sputtered TiB<sub>2</sub> intended for tribological applications, *Surf. Coat. Technol.* 124 (2000) 253–261, [https://doi.org/10.1016/S0257-8972\(99\)00638-6](https://doi.org/10.1016/S0257-8972(99)00638-6).
- [2] F. Lofaj, T. Moskalewicz, G. Cempura, M. Mikula, J. Dusza, A. Czyska-Filemonowicz, Nanohardness and tribological properties of nc-TiB<sub>2</sub> coatings, *J. Eur. Ceram. Soc.* 33 (2013) 2347–2353, <https://doi.org/10.1016/j.jeurceramsoc.2013.02.024>.
- [3] M. Mikula, B. Granić, T. Roch, T. Plecenik, I. Vávra, E. Dobročka, A. Šatka, V. Bursíková, M. Držík, M. Zahoran, A. Plecenik, P. Kús, The influence of low-energy ion bombardment on the microstructure development and mechanical properties of TiB<sub>x</sub> coatings, *Vacuum*. 85 (2011) 866–870, <https://doi.org/10.1016/j.vacuum.2010.12.011>.
- [4] J. Thörnberg, J. Palisaitis, N. Hellgren, F.F. Klimashin, N. Ghafoor, I. Zhirkov, C. Azina, J. Battaglia, A. Kusiak, M.A. Sortica, J.E. Greene, L. Hultman, I. Petrov, P. O.Å. Persson, J. Rosen, Microstructure and materials properties of understoichiometric TiB<sub>x</sub> thin films grown by HIPIMS, *Surf. Coatings Technol.* 404 (2020), 126537, <https://doi.org/10.1016/j.surfcoat.2020.126537>.
- [5] R.G. Munro, Material properties of titanium diboride, *J. Res. Natl. Inst. Stand. Technol.* 105 (2000) 709–720, <https://doi.org/10.6028/jres.105.057>.
- [6] A.D. McLeod, J.S. Haggerty, D.R. Sadoway, Electrical resistivity of monocrystalline and polycrystalline TiB<sub>2</sub>, *J. Am. Ceram. Soc.* 67 (1984) 705–708.
- [7] A.S. Dranenkov, V.A. Lavrenko, V.N. Talash, Corrosion resistance of nanostructured TiB<sub>2</sub> films in 3% NaCl solution, *Powder Metall. Met. Ceram.* 49 (2010) 174–178, <https://doi.org/10.1007/s11106-010-9218-4>.
- [8] I.I. Korobov, G.V. Kalinnikov, A.V. Ivanov, N.N. Dremova, R.A. Andrievski, S. P. Shilkin, Corrosion resistance of nanostructured films of titanium diboride in mineral acid solutions, *Prot. Met. Phys. Chem. Surfaces*. 52 (2016) 618–621, <https://doi.org/10.1134/S2070205116040171>.
- [9] B.R. Golla, T. Bhandari, A. Mukhopadhyay, B. Basu, Titanium diboride, in: W. G. Fahrenholtz, E.J. Wuchina, W.E. Lee, Y. Zhou (Eds.), *Ultra-High Temp. Ceram. Mater. Extrem. Environ. Appl.*, Wiley, Hoboken, NJ, 2014, pp. 316–360, <https://doi.org/10.1002/9781118700853.ch13>.
- [10] M. Berger, S. Hogmark, Evaluation of TiB<sub>2</sub> coatings in sliding contact against aluminium, *Surf. Coat. Technol.* 149 (2002) 14–20, [https://doi.org/10.1016/S0257-8972\(01\)01361-5](https://doi.org/10.1016/S0257-8972(01)01361-5).
- [11] Y. Mu, K. Chen, W.J. Meng, F. Mei, Low temperature deposited titanium boride thin films and their application to surface engineering of microscale mold inserts, *Microsyst. Technol.* 18 (2012) 667–677, <https://doi.org/10.1007/s00542-012-1465-5>.
- [12] M. Ma, Large scale PVD hard coating process for tribological applications, in: *Proc. 46<sup>th</sup> Annu. Soc. Vac. Coaters Conf.*, 2003, p. 535.
- [13] W.G. Fahrenholtz, E.J. Wuchina, W.E. Lee, Y. Zhou (Eds.), *Ultra-High Temperature Ceramics: Materials for Extreme Environment Applications*, Wiley, Hoboken, NJ, 2014.
- [14] P.H. Mayrhofer, C. Mitterer, J.G. Wen, J.E. Greene, I. Petrov, Self-organized nanocolumnar structure in superhard TiB<sub>2</sub> thin films, *Appl. Phys. Lett.* 86 (2005) 1–3, <https://doi.org/10.1063/1.1887824>.
- [15] F. Kunc, J. Musil, P.H. Mayrhofer, C. Mitterer, Low-stress superhard Ti–B films prepared by magnetron sputtering, *Surf. Coat. Technol.* 174–175 (2003) 744–753, <https://doi.org/10.1016/S0257-8972>.
- [16] J. Neidhardt, S. Mráz, J.M. Schneider, E. Strub, W. Bohné, B. Liedke, W. Möller, C. Mitterer, Experiment and simulation of the compositional evolution of Ti–B thin films deposited by sputtering of a compound target, *J. Appl. Phys.* 104 (2008), <https://doi.org/10.1063/1.2978211>.
- [17] I. Petrov, A. Hall, A.B. Mei, N. Nedfors, I. Zhirkov, J. Rosen, A. Reed, B. Howe, G. Greczynski, J. Birch, L. Hultman, J.E. Greene, Controlling the boron-to-titanium ratio in magnetron-sputter-deposited TiB<sub>x</sub> thin films, *J. Vac. Sci. Technol. A Vacuum, Surfaces, Film.* 35 (2017), 050601, <https://doi.org/10.1116/1.4982649>.
- [18] N. Nedfors, D. Primetzhofer, I. Zhirkov, J. Palisaitis, P.O.Å. Persson, J.E. Greene, I. Petrov, J. Rosen, The influence of pressure and magnetic field on the deposition of epitaxial TiB<sub>x</sub> thin films from DC magnetron sputtering, *Vacuum*. 177 (2020), 109355, <https://doi.org/10.1016/j.vacuum.2020.109355>.
- [19] N. Hellgren, J. Thörnberg, I. Zhirkov, M.A. Sortica, I. Petrov, J.E. Greene, L. Hultman, J. Rosen, High-power impulse magnetron sputter deposition of TiB<sub>x</sub> thin films: effects of pressure and growth temperature, *Vacuum*. 169 (2019), 108884, <https://doi.org/10.1016/j.vacuum.2019.108884>.
- [20] *Atomic, molecular, and optical physics; ionization potentials of atoms and atomic ions*, in: D.R. Lide (Ed.), *CRC Handb. Chem. Phys.*, 84th ed., CRC, Boca Raton, FL, 2003.
- [21] B. Bakhit, I. Petrov, J.E. Greene, L. Hultman, J. Rosén, G. Greczynski, Controlling the B/Ti ratio of TiB<sub>x</sub> thin films grown by high-power impulse magnetron sputtering, *J. Vac. Sci. Technol. A Vacuum, Surfaces, Film.* 36 (2018), 030604, <https://doi.org/10.1116/1.5026445>.
- [22] J. Palisaitis, M. Dahlqvist, A.J. Hall, J. Thörnberg, I. Persson, N. Nedfors, J. E. Greene, I. Petrov, J. Rosen, P. Persson, Where is the unmatched transition metal in substoichiometric diboride line compounds? *Acta Mater.* 204 (2021), 116510, <https://doi.org/10.1016/j.actamat.2020.116510>.
- [23] J. Palisaitis, Use of cleaved wedge geometry for plan-view transmission electron microscopy sample preparation, *Microsc. Res. Tech.* (2021) 1–9, <https://doi.org/10.1002/jemt.23876>.
- [24] G. Greczynski, D. Primetzhofer, J. Lu, L. Hultman, Core-level spectra and binding energies of transition metal nitrides by non-destructive X-ray photoelectron spectroscopy through capping layers, *Appl. Surf. Sci.* 396 (2017) 347–358.
- [25] G. Greczynski, L. Hultman, Towards reliable X-ray photoelectron spectroscopy: sputter-damage effects in transition metal borides, carbides, nitrides, and oxides, *Appl. Surf. Sci.* 542 (2021), 148599.
- [26] N. Hellgren, G. Greczynski, M.A. Sortica, I. Petrov, L. Hultman, J. Rosen, X-ray photoelectron spectroscopy analysis of TiB<sub>x</sub> (1.3 ≤ x ≤ 3.0) thin films, *J. Vac. Sci. Technol. A Vacuum, Surfaces, Film.* 023403 (2021), 023403, <https://doi.org/10.1116/6.0000789>.
- [27] W.C. Oliver, G.M. Pharr, An improved technique for determining hardness and elastic modulus experiments, *J. Mater. Res.* 7 (1992) 1564.
- [28] S.P. Dodd, M. Cankurtaran, Ultrasonic determination of the temperature and hydrostatic pressure dependences of the elastic properties of ceramic titanium diboride, 6 (2001) 3989–3996.
- [29] W. Gust, A.C. Holt, E.B. Royce, Dynamic yield, compressional, and elastic parameters for several lightweight intermetallic compounds, *J. Appl. Phys.* 44 (1973) 550, <https://doi.org/10.1063/1.1662224>.
- [30] D.E. Wiley, W.R. Manning, O. Hunter Jr., Elastic properties of polycrystalline TiB<sub>2</sub>, ZrB<sub>2</sub> and HfB<sub>2</sub> from room temperature to 1300 °K, *J. Less Common Met.* 18 (1969) 149–157, [https://doi.org/10.1016/0022-5088\(69\)90134-9](https://doi.org/10.1016/0022-5088(69)90134-9).
- [31] A.C. Fischer-Cripps, Critical review of analysis and interpretation of nanoindentation test data, *Surf. Coat. Technol.* 200 (2006) 4153–4165, <https://doi.org/10.1016/j.surfcoat.2005.03.018>.
- [32] Y.-Y. Chen, J.-Y. Juang, Finite element analysis and equivalent parallel-resistance model for conductive multilayer thin films, *Meas. Sci. Technol.* 27 (2016), 074006, <https://doi.org/10.1088/0957-0233/27/7/074006>.
- [33] T.A. Parthasarathy, A Model for the Oxidation of ZrB<sub>2</sub>, HfB<sub>2</sub> and TiB<sub>2</sub> 55, 2007, pp. 5999–6010, <https://doi.org/10.1016/j.actamat.2007.07.027>.
- [34] C. Huber, S.S. Jahromy, C. Jordan, M. Schreiner, M. Harasek, A. Werner, F. Winter, Boric acid: a high potential candidate for thermochemical energy storage, *Energies*. 12 (2019) 1086, <https://doi.org/10.3390/en12061086>.
- [35] J. Thörnberg, B. Bakhit, J. Palisaitis, N. Hellgren, L. Hultman, G. Greczynski, P.O. Å. Persson, I. Petrov, J. Rosen, Improved oxidation properties from a reduced B content in sputter-deposited TiB<sub>x</sub> thin films, *Surf. Coat. Technol.* 420 (2021), 127353, <https://doi.org/10.1016/j.surfcoat.2021.127353>.
- [36] D. Lide, ed., *Properties of the Elements and Inorganic Compounds*, in: *CRC Handb. Chem. Phys.*, 84th ed., CRC, Boca Raton, FL, 2003.
- [37] A.L. Patterson, The Scherrer formula for X-ray particle size determination, *Phys. Rev.* 56 (1939) 978, <https://doi.org/10.1103/PhysRev.56.978>.
- [38] M. Mikula, B. Granić, V. Bursíková, A. Csaba, M. Držík, S. Kavecký, A. Plecenik, P. Kús, Mechanical properties of superhard TiB<sub>2</sub> coatings prepared by DC magnetron sputtering, *Vacuum*. 82 (2007) 278–281, <https://doi.org/10.1016/j.vacuum.2007.07.036>.
- [39] N. Kalfagiannis, G. Volonakis, L. Tsetseris, S. Logothetidis, Excess of boron in TiB<sub>2</sub> superhard thin films: a combined experimental and ab initio study, *J. Phys. D. Appl. Phys.* 44 (2011), <https://doi.org/10.1088/0022-3727/44/38/385402>.
- [40] M. Rahman, C.C. Wang, W. Chen, S.A. Akbar, C. Mroz, Electrical resistivity of titanium diboride and zirconium diboride, *J. Am. Ceram. Soc.* 78 (1995) 1380–1382, <https://doi.org/10.1111/j.1151-2916.1995.tb08498.x>.
- [41] A. Shutou, T. Matsui, H. Tsuda, H. Mabuchi, K. Morii, Structural and electric properties of TiB<sub>2</sub> thin films by RF sputtering, *Mater. Lett.* 45 (2000) 143–148.
- [42] B. Todorović, T. Jokić, Z. Rakočević, Z. Marković, B. Gaković, T. Nenadović, The effect of rapid thermal annealing on structural and electrical properties of TiB<sub>2</sub> thin films, *Thin Solid Films* 300 (1997) 272–277, [https://doi.org/10.1016/S0040-6090\(96\)09458-8](https://doi.org/10.1016/S0040-6090(96)09458-8).